

Heterarchical modelling of comminution for rotary mills: Part II — Particle crushing with segregation and mixing

Mukesh Singh Bisht

The University of Sydney

François Guillard

The University of Sydney

Paul Shelley

Molycop Innovation

Benjy Marks

The University of Sydney

Itai Einav (✉ itai.einav@sydney.edu.au)

The University of Sydney

Research Article

Keywords: Comminution, Segregation, Mixing, Particle size distribution, Hierarchy, Rotary mills

Posted Date: February 13th, 2024

DOI: <https://doi.org/10.21203/rs.3.rs-3938203/v1>

License:  This work is licensed under a Creative Commons Attribution 4.0 International License.

[Read Full License](#)

Additional Declarations: No competing interests reported.

Heterarchical modelling of comminution for rotary mills: Part II — Particle crushing with segregation and mixing

Mukesh Singh Bisht^{1,2}, François Guillard¹, Paul Shelley², Benjy Marks¹,
Itai Einav^{1*}

¹School of Civil Engineering, The University of Sydney, Sydney, 2006, NSW, Australia.

² Molycop Innovation, Molycop, Omaha, 68106, Nebraska, USA.

*Corresponding author(s). E-mail(s): itai.einav@sydney.edu.au;

Contributing authors: mukesh.bisht@sydney.edu.au; francois.guillard@sydney.edu.au;
paul.shelley@molycop.com; benjy.marks@sydney.edu.au;

Abstract

In granular media, the crushing of individual particles is influenced by the number of contacts with neighbouring particles. This well-known phenomenon of “cushioning” shields the individual particles from crushing when the number of contacts is high. However, in open systems that involve extensive granular flow and bulk motion, like those found in industrial mills, the neighbouring particles continually exchange positions due to segregation and mixing, thereby altering the number of neighbouring contacts and their sizes, affecting the crushing of individual particles. Therefore, a critical challenge for properly modelling comminution in such systems lies in tracking the fluxes of the various particle size classes. Here, we explore the physics that governs the mechanisms of segregation and mixing within the multiscale heterarchical modelling paradigm. Building upon the framework developed in Part I, which integrated the heterarchical aspects of the physics of crushing along streamlines, we further account for segregation and mixing, and demonstrate their impact on the comminution efficiency of autogenous grinding mills. In particular, segregation is shown to greatly enhance the extent of particle crushing within the mill. Accordingly, we posit that this mechanism cannot be ignored. In summary, the new model sheds light on previously obscured dynamics within industrial mills, as well as enables the field to predict the time evolution of the particle size distribution at any point in the mill domain. This modelling capability opens the doors to new developments for estimating and improving milling efficiencies.

Keywords: Comminution, Segregation, Mixing, Particle size distribution, Hierarchy, Rotary mills

1 Introduction

Granular materials often segregate by size or density when flowing. This segregation is typically not perfect, and some level of mixing is present counteracting this segregation. These two competing mechanisms create patterns in terms of the spatial distributions of size or density of particles. When

particles also can crush, these patterns can become more pronounced and complex. The mechanisms of particle segregation, mixing, and crushing have many important implications for different natural and industrial processes. The purpose of this paper is to address the coupling between these mechanisms within the context of particle milling.

In natural granular flows such as fault gauges [1, 2], snow avalanches [3], debris flows [4, 5], and rock avalanches [6, 7], particle segregation is a key mechanism driving the dynamics of particle sizes. Segregation is also responsible for stratification in several rock formations [8]. The process of segregation in granular flows has been extensively studied, and various theories have been developed to model the behaviour of mixtures of two [9–12] or more [13–20] types of particles. These models describe segregation in simplified flow geometries, such as inclined planes [15, 16, 18], which is somewhat representative of granular avalanches, landslides, and debris flows where segregation occurs in the direction normal to the flow [21]. Other models have focused on the fronts of these avalanches [22]. Recently, models have been proposed for bounded heap flow, rotating tumblers, and hopper discharge [17, 19, 20].

In addition to segregation, another significant mechanism that occurs during granular flows is the mixing of particles. Indeed, complete segregation where particle species are fully separated from one another is rarely observed due to the random fluctuations of particles during the flow, which act as a de-segregation mechanism. In the past, the phenomenon of mixing has been studied analytically [12, 23, 24] and explored using experiments and numerical simulations [19, 25, 26].

In this work, we will focus on the modelling of the interior of autogenous grinding (AG) mills, where the particles undergo substantial deformations. AG mills are specifically designed to produce severe particle crushing, as first described in Part I of this contribution. In this Part II, we additionally explain the physics of the segregation and mixing mechanisms within the heterarchical stochastic formalism and study the effects of segregation and mixing on the system.

In Part I of this contribution, we delved into the dominant mechanism of kinetic crushing, which is prevalent in industrial mills. However, that paper highlighted the clear necessity to further treat the segregation and mixing mechanisms as part of the modelled process of comminution. By solely relying on kinetic crushing, the extent of crushing within the system diminished over time, as individual particles do not explore the whole system, but instead follow closed streamlines through the mill and reach a state where they are cushioned against further crushing. In

practice, however, this cushioning is disturbed by segregation and mixing. The significance of this point is thoroughly examined in this Part II of the study.

In summary, Part I of this study presented two of the three novel contributions of this two-part study: (i) the introduction of the kinetic crushing model within the heterarchical framework, and (ii) the novel scheme of integrating the heterarchical crushing model along streamlines to study comminution in rotary mills. In this Part II, we present the third novel contribution of (iii) tessellating the material within the mill domain for equal mass material points along streamlines to investigate the mixing and segregation of particles within rotary mills. By combining the crushing capabilities of the heterarchical framework developed in part I with the new capabilities in capturing segregation and mixing, the heterarchical streamline approach is here used to study their complex interplay during comminution in an AG mill.

This paper is organised as follows. Firstly, we describe the novel stochastic heterarchical approach for solving the continuum equations for segregation and mixing mechanisms. Secondly, we use the heterarchical approach to simulate bidisperse segregation and mixing on both structured and unstructured grids, and validate our approach against analytical solutions for equivalent continuum equations available in the literature. Thirdly, we calibrate the model parameters using experimental results for segregation and mixing in a rotating drum. Fourthly, we implement the model for the AG mill, activating all three particle size evolution mechanisms simultaneously, *i.e.* crushing, segregation, and mixing. The results are then used to provide a new comprehensive understanding for the comminution process that develops within AG mills. Finally, we discuss the potential applications of this new model, its limitations, and perspectives for the future.

2 Segregation and Mixing

Segregation and mixing are open-system processes, which are tightly linked to the advection of particles in space. This is contrasted with the mechanism of crushing, which instead is seen as a closed-system process. The general heterarchical

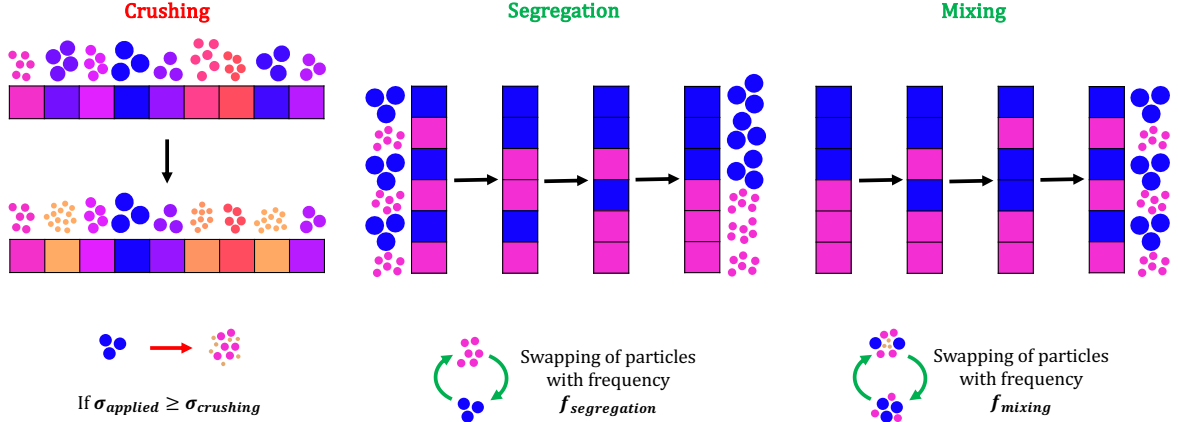


Fig. 1: The stochastic rules for crushing, segregation, and mixing mechanisms in the general heterarchical framework. The crushing rule is applied along the internal micro-structural coordinate while the rules for segregation and mixing are applied along the physical external coordinate(s). This figure shows the evolution of the initial state over time when the rules for crushing, segregation, and mixing are applied (colour figure online).

113 framework [18] outlines the rules for the segrega- 142
 114 tion and mixing of particles in space, which are
 115 briefly discussed here.

116 As described in [18] and in Part I of this
 117 contribution, in the heterarchical framework a
 118 polydisperse granular system (*i.e.* one composed
 119 of many particle sizes) is replaced by an equiv-
 120 alent stochastic lattice. Each cell in the lattice
 121 represents particles of a specific size and the
 122 position of a cell in the lattice is defined by
 123 both external physical coordinates and an internal
 124 micro-structural coordinate. The rule for crush-
 125 ing is applied along the internal micro-structural
 126 coordinate and the advective rules of segregation
 127 and mixing are applied along the external physical
 128 coordinates. The rules for segregation and mixing
 129 are such that the particle size in a given cell of
 130 the lattice is swapped with the particle size of its
 131 neighbouring cells with a certain frequency (see
 132 Fig. 1). While the direction of the swapping of par-
 133 ticle sizes is random for the mixing process, it is
 134 dependent on the neighbouring particle sizes for
 135 the segregation process.

136 In this section, we present the mathemati-
 137 cal formulation for implementing the particle size
 138 dynamics of segregation and mixing in rotary
 139 mills using the heterarchical model. The formula-
 140 tion is presented for a polydisperse particle size
 141 distribution.

2.1 Particle size distribution

It is useful to represent a polydisperse granular medium using a continuum particle size coordinate s [15]. The fraction of particle sizes in the range ($s_a < s < s_b$) can then be calculated as

$$\Phi(s_a < s < s_b) = \int_{s_a}^{s_b} \phi(s') ds', \quad (1)$$

where ϕ is the probability density function that characterises the particle size distribution, such that

$$\int \phi ds = 1, \quad \bar{s} = \int s \phi ds, \quad (2)$$

while \bar{s} is the average particle size.

2.2 Density

When dealing with polydisperse media, it is also useful to define three different forms of density other than the density of the material (ρ_m). The intrinsic density $\rho^*(s)$ represents the mass of a unit volume of particle size s . On the other hand, the partial density $\rho(s)$ signifies the contribution of the intrinsic density of a given particle size s towards the average (or bulk) density ρ_b . The relationships between those densities are given by:

$$\rho^* = \rho_m \nu, \quad \rho = \rho^* \phi, \quad \rho_b = \int \rho ds, \quad (3)$$

145 where ν is the solid fraction.

146 2.3 Conservation of mass

The governing equation for the conservation of mass [27] of a given class of particle sizes, in the reference frame of the barycentric motion (i.e. having already accounted for the bulk motion of the material) can be expressed as

$$\frac{\partial \rho}{\partial t} + \nabla \cdot \vec{F}(\rho) = 0, \quad (4)$$

where $\vec{F}(\rho)$ is the corresponding mass flux, which is generally given by

$$\vec{F}(\rho) = \rho \hat{u} + D \nabla \rho. \quad (5)$$

147 Notice that the mass flux consists of two components, the advective flux ($\vec{F}_s = \rho \hat{u}$) and the
148 diffusive flux ($\vec{F}_m = D \nabla \rho$), where \hat{u} is the segregation
149 velocity and D is the granular diffusivity in
150 the system.

151 The segregation velocity of particles [9, 11,
152 15, 17, 19] has been shown to be a function
153 of at least the shear strain rate, particle size
154 ratio, concentration of the particle sizes, particle
155 shape and density. Existing segregation models
156 typically consider particle segregation driven by
157 either the contrast in their size or density. Most
158 of these models cannot capture the segregation
159 behaviour when both the particle size and the par-
160 ticle density vary. As an alternative, [28] proposed
161 a framework to explain the segregation behaviour
162 in granular flows using the granular temperature
163 and the kinetic pressure, which are functions of
164 the measurable velocity fluctuation of the parti-
165 cles. The gradient of the granular temperature, or
166 of the associated kinetic pressure, can be used to
167 explain the direction and the rate of segregation
168 in systems where both particle size and particle
169 density vary. Building upon this concept [29] have
170 expressed the segregation velocity as a function of
171 the kinetic pressure (p_k) through

$$\hat{u} = \frac{1 - \overline{s^{-1}}}{\rho_b c_o} \nabla p_k, \quad (6)$$

172 where c_o is a parameter controlling the rate of
173 segregation, and $\overline{s^{-1}}$ is the local harmonic average
174 particle size. This harmonic average particle size
175 is a weighted average with respect to the partial

density (ρ) of each particle size (s) and is given as

$$\overline{s^{-1}} = \frac{\int \rho(s') ds'}{\int \frac{\rho(s')}{s'} ds'}. \quad (7)$$

The expression in Eq. 6 allows us to calculate the segregation velocity for any arbitrary particle size in a polydisperse granular system. For the current case of an AG mill (where only mineral particles exist), by assuming that all the particles have the same intrinsic density, the above expression can be simplified to

$$\overline{s^{-1}} = \left(\int \frac{\phi(s')}{s'} ds' \right)^{-1}. \quad (8)$$

Following the work of [30, 31], the diffusivity (D) can be calculated as

$$D = l \bar{s}^2 |\dot{\varepsilon}_s| / \sqrt{I}, \quad (9)$$

152 where l is a non-dimensional parameter controlling
153 the rate of diffusivity, $\dot{\varepsilon}_s$ is the shear strain rate,
154 $I = \dot{\varepsilon}_s \bar{s} \sqrt{\rho_m / P}$ is the inertial number [32] previ-
155 ously defined in Part I of the contribution, and P
156 is the total pressure.

2.4 Stochastic swapping rules

157 As detailed in Part I of this two-part contribu-
158 tion, the comminution problem within rotary mills
159 is tackled by integrating the physics dictating the
160 particle size dynamics along a set of closed set of
161 streamlines. This set is taken consistently from a
162 known velocity field, obtained either analytically if
163 such an equation is available or by coarse-graining
164 particle-based simulations. These streamlines are
165 then discretised into equal mass material points
166 along the length of the streamlines, consistent
167 with discrete time steps. The volume (assuming a
168 unit length into the page) corresponding to these
169 material points is obtained using a Voronoi tessel-
170 lation [33] as shown in Fig. 2. The mass balance
171 equation (Eq. 4) is solved for each of these material
172 points at each time step.

173 For a given material point (i, j) and particle
174 size (s), Eq. 4 can be written as

$$\frac{\partial \rho_{i,j,s}}{\partial t} + \nabla \cdot \vec{F}(\rho_{i,j,s}) = 0, \quad (10)$$

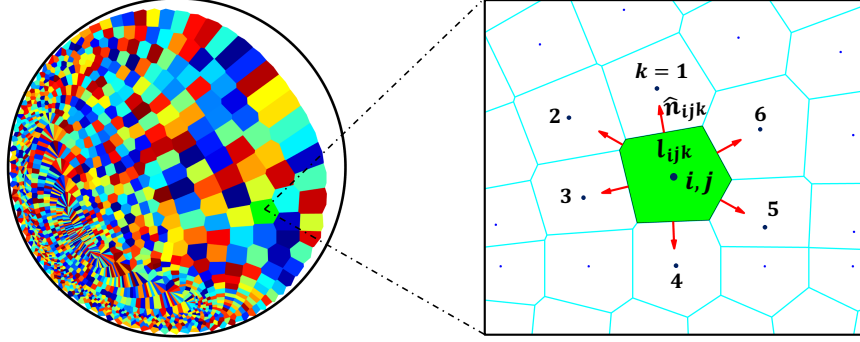


Fig. 2: Tessellation of space and flux calculation of material points for the segregation and mixing mechanisms in the mill. *Left:* The space around each material point is discretised by a Voronoi tessellation. The areas are coloured randomly. *Right:* The flux of material moves in and out of a given cell to its neighbouring cells through the sides of the Voronoi cell. The highlighted cell in this figure has six neighbouring cells numbered from $k = 1$ to 6, where \hat{n}_{ijk} is the unit normal vector on each side of the polygon and l_{ijk} is the corresponding length of the side of the polygon (colour figure online).

where $\rho_{i,j,s}$ is the discretised array of partial densities. Upon integrating the above equation over the volume of a material point, we get

$$\int_V \frac{\partial \rho_{i,j,s}}{\partial t} dv + \int_V \nabla \cdot \vec{F}(\rho_{i,j,s}) dv = 0. \quad (11)$$

Using the Gauss divergence theorem, the second term in the Eq. 11 can be written to give

$$\int_V \frac{\partial \rho_{i,j,s}}{\partial t} dv + \oint_S (\vec{F}(\rho_{i,j,s}) \cdot \hat{n}) ds = 0, \quad (12)$$

where \hat{n} is the surface unit normal. Assuming that the density within a given cell is homogeneous, we thus find

$$\frac{\partial \rho_{i,j,s}}{\partial t} = -\frac{1}{V_{i,j}} \oint_S (\vec{F}(\rho_{i,j,s}) \cdot \hat{n}) ds. \quad (13)$$

We approximate the surface integral (\oint_S) by a summation (Σ) over the sides of the Voronoi polygons. Accordingly, Eq. 13 becomes

$$\frac{\partial \rho_{i,j,s}}{\partial t} = -\frac{1}{V_{i,j}} \sum_k (\vec{F}(\rho_{i,j,s}) \cdot \hat{n}_{ijk}) l_{ijk}, \quad (14)$$

where the index k denotes the edges of a Voronoi polygon with its neighbouring cells, l_{ijk} is the length of the corresponding sides of the polygon, and $V_{i,j}$ is the volume of the polygon.

The frequency of swapping particle sizes s along the k^{th} edge of the Voronoi polygon with its

neighbouring cell is then defined as

$$f_{i,j,s,k}^{swap} = \frac{l_{ijk}}{\rho^* V_{i,j}} (\vec{F}_{i,j,s} \cdot \hat{n}_{ijk}). \quad (15)$$

Notice that the mass flux ($\vec{F}_{i,j,s}$) in the above equation consists of two components, advective flux and diffusive flux as defined in Eq. 5. For the purpose of calculating the diffusive flux ($\vec{F}_{m_{\{i,j,s\}}}$), we require a measure of the spatial gradient of the particle size distribution. To obtain this gradient, we approximate the particle size distribution at any material point by a histogram of particle sizes discretised into N_g bins spaced logarithmically. In general, there are many ways to determine an adequate number of bins for a given histogram. We must discretise M heterarchical cells into N_g bins, and choose $N_g = \text{int}(\sqrt{M})$, where int represents rounding to the nearest integer.

The solid fraction for a given size bin $\Phi(s_a < s < s_b)$ can be calculated from Eq. 1. This is done for every grainsize coordinate in the histogram and across all the material points in the mill domain. Note that we have used the term ‘grainsize coordinate’ [18] to describe the discretization of the particle size distribution within a given material point and this highlights its role as an internal coordinate in a continuum framework.

The gradient of the solid fraction can thus be obtained for the N_g bins in space, which is then interpolated to obtain the corresponding value of $\vec{F}_{m_{\{i,j,s\}}}$ for any particle size s .

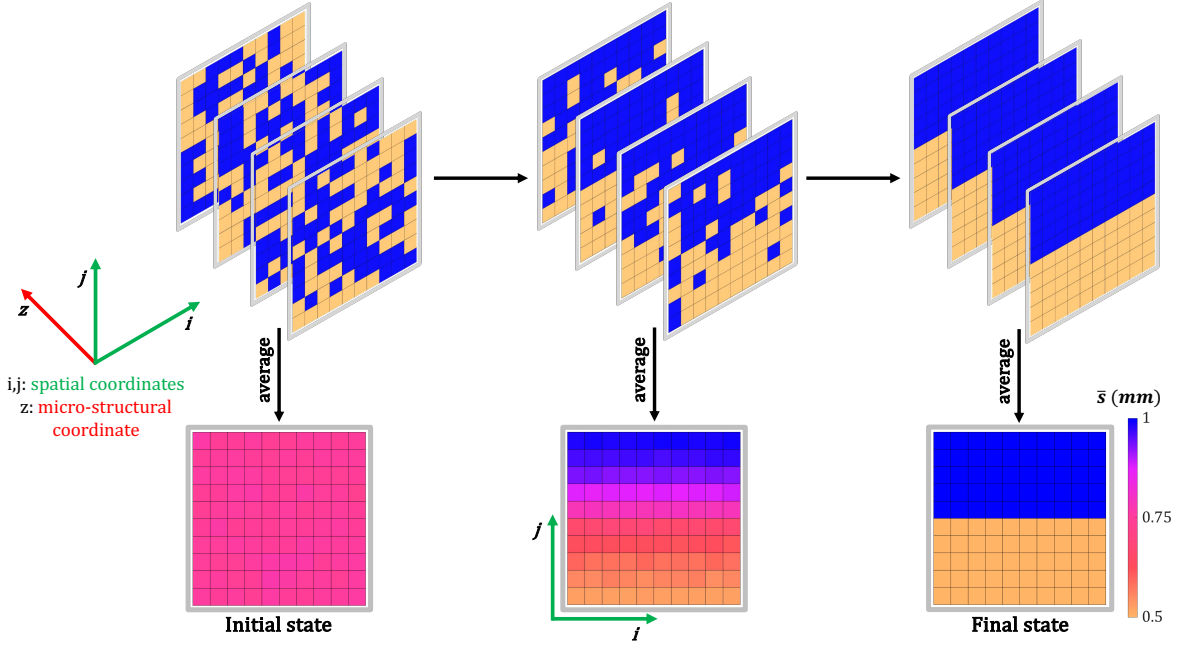


Fig. 3: Bidisperse segregation in a structured lattice. An regular lattice is randomly filled with small (yellow) and large (blue) particles in equal proportion. A number of such lattices are considered along the heterarchical coordinate as shown in the *left*. The particle size is averaged along the heterarchical coordinate for each cell. The rule for segregation is applied to this lattice and as segregation takes place we achieve a completely segregated state as shown in *right*. The animation showing the evolution of average particle size from initial uniform to a perfectly segregated state can be found in SI Video 1 (colour figure online).

Once the frequency of swapping is obtained, we need to determine the probability with which the particle sizes are swapped in a given time increment Δt . The probability of swapping a particle size in a Voronoi volume along a neighbouring cell from one of its edges is obtained as

$$P_{i,j,s,k} = \langle f_{i,j,s,k}^{swap} \rangle \Delta t_c, \quad (16)$$

where $\langle \rangle$ is the Macaulay function (defined as $\langle x \rangle = x$ for $x \geq 0$, and $\langle x \rangle = 0$ for $x < 0$). Note that the expression for swapping frequency in Eq. 15 also carries a direction that is embedded in its sign. We choose to only propagate material in the positive direction and use the Macaulay function to satisfy this requirement. This is justified as the frequencies that have a negative direction for the current cell, will be taken care of in the adjacent cells where they will have a positive direction. A critical time step (Δt_c) is chosen such

that the maximum of the probabilities of swapping particles along the neighbouring cells is less than unity. Here, we denote this critical time step as $\max_k (f_{i,j,s,k}^{swap}) \Delta t_c = \frac{1}{2}$ to ensure stability of the system.

For each cell, one of the edges where swapping is susceptible to occur is selected based on the relative weight of that edge on the total probability $P_{i,j,s,k} / \sum_k P_{i,j,s,k}$. A random number is then drawn and the swapping is effectively performed if the number is below $P_{i,j,s,k}$. This ensures that at most one swap occurs on any given cell for each timestep.

3 Numerical validation

In the previous section, we defined a numerical scheme for unstructured grids to account for the heterarchical physics governing the mechanism of segregation and mixing. In this section, we validate the new numerical scheme against existing

analytical solutions from the literature [9, 11, 12], as well as solutions using an alternative numerical scheme for systems that can be represented by regular grids by [18, 34].

We validate the system with bidisperse particles and consider the mechanisms of segregation and mixing independently. We simulate a simple system with two spatial dimensions in a square domain. Initially, we consider a structured lattice in which every cell has an identical volume. Subsequently, we extend this analysis to an unstructured lattice where the cell volume varies in space.

3.1 Structured lattice

3.1.1 Segregation

We begin with a regular square lattice, with each cell randomly filled with either small particles ($s_a = 0.5$ mm) or large particles ($s_b = 1$ mm) in equal proportion. A number of such lattices are considered along the heterarchical coordinate, as shown in Fig. 3. The average particle size at a given cell location in physical space is obtained by averaging all of the particle sizes along the heterarchical coordinate, as defined by $\bar{s}_{i,j} = \frac{1}{M} \sum_{z=1}^M s_{i,j,z}$. We set an initial condition such that the average particle size at each cell location in the physical space is uniform and the mass of particles in each cell is equal. Another condition on the segregation rule is implemented for a simple case where the gradient of kinetic pressure in space is constant and is given as $\nabla p_k = 1\hat{j}$ N/m³, where \hat{j} is the unit vector along the vertical spatial coordinate j . The parameter c_0 in Eq. 6 is here taken as 1 s⁻¹ for simplicity. The boundary condition is set such that the advective flux ($\vec{F}_s = \rho\hat{u}$) is zero for the top and bottom cells of the lattice. Neighbouring cells swap particle sizes with a frequency that is given by Eq. 15.

Fig. 3 shows the initial and final states after the segregation is completed. After some time, as the particles begin to segregate, they gradually develop into a state where all the large particles are found at the top of the lattice, while the smaller ones reside at the bottom.

A spatiotemporal plot of the average particle size over time along the physical vertical direction is also shown in Fig. 4 for varying values of M .

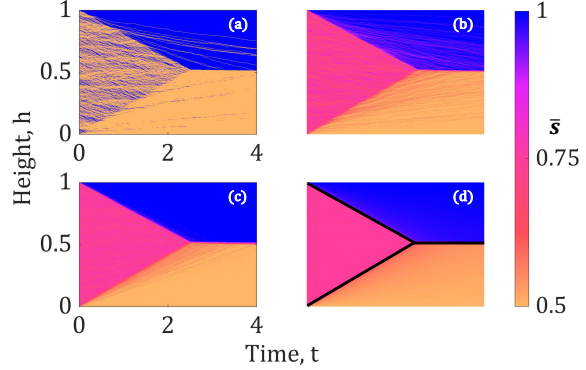


Fig. 4: Time evolution of average particle size (\bar{s}) in a structured lattice for bidisperse segregation with varying the number of cells (M) along the heterarchical coordinate. For each case, the gradient of kinetic pressure field $\nabla p_k = 1\hat{j}$ N/m³ and the lattice consists of 100 × 100 cells along the two spatial coordinates. From (a) to (d) the number of cells along the heterarchical coordinate are varied as $M = 1, 10, 10^2$ and 10^3 . As the number of cells along the heterarchical coordinate increases the solution converges to the equivalent analytical solution of the 1D advection equation (Eq. 17) (colour figure online).

As the averaging is done over an increasing number of cells along the heterarchical coordinate, the spatiotemporal plot converges to the analytical solution given in [9, 11], as also shown in [18, 34]. The concentration shocks as seen in the bottom right of Fig. 4 represent the analytic solution (the superimposed black lines) of the following partial differential equation

$$\frac{\partial \phi}{\partial t} = \frac{\partial}{\partial z}(\phi\hat{u}). \quad (17)$$

3.1.2 Mixing

To validate the mixing mechanism, we take the same lattice as above, but initialise the simulations with a perfectly segregated state where the cells in the top half of the lattice are entirely composed of large particles, and small particles in the bottom half. The diffusivity (D) is assumed to be constant in this case for simplicity. The boundary condition is set such that the diffusive flux ($\vec{F}_m = D\nabla\rho$) is zero for the top and bottom cells of the lattice.

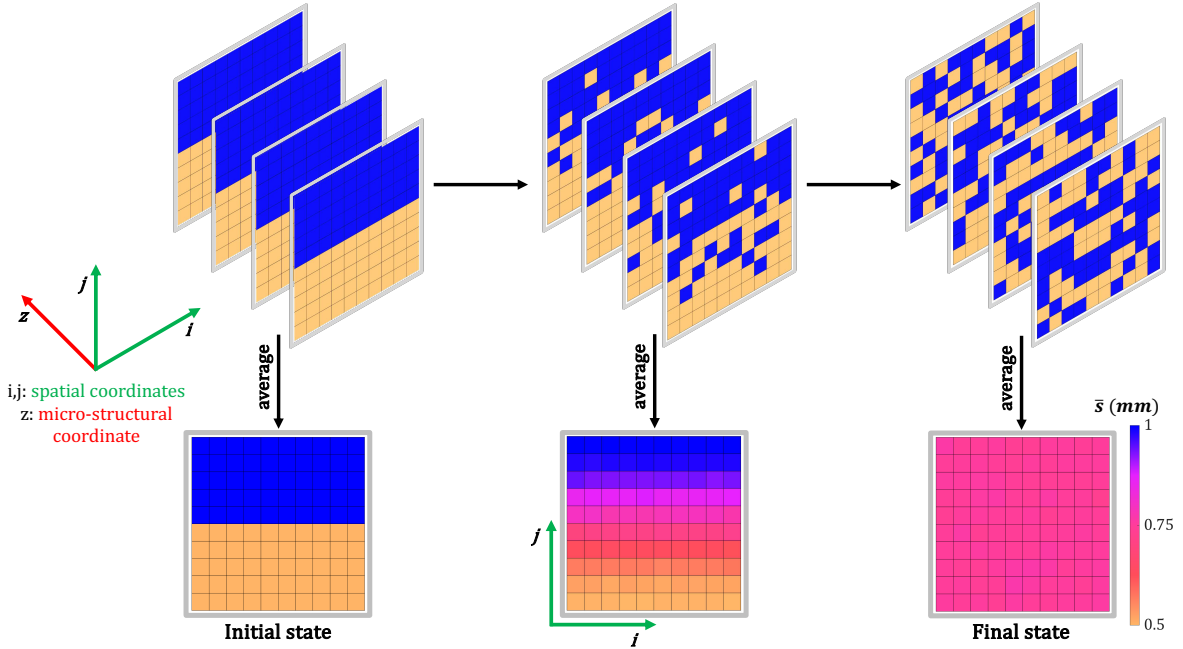


Fig. 5: Bidisperse mixing in a structured lattice. An initial uniform lattice is filled in equal proportion with small (yellow) and large (blue) particles. A number of such lattices are considered along the heterarchical coordinate as shown in the *left*. The particle size is averaged along the heterarchical coordinate for each cell. The rule for mixing is applied for this lattice and as the particles mix we achieve a complete uniform state from an initial perfectly segregated state as shown in *right*. The animation showing the evolution of average particle size from the initial perfectly segregated state to a uniform state can be found in SI Video 2 (colour figure online).

289 Fig. 5 shows the initial completely segregated 297 state and the final state after which the particle 298 sizes are uniformly distributed throughout space 299 due to mixing. This represents a system in which 300 cells undergo Fickian diffusion [24].

A spatiotemporal plot of the average particle 302 size with time along the physical coordinate in the 303 vertical direction is shown in Fig. 6. Similar to the 304 case of segregation, as the averaging is done over 305 an increasing number of cells along the heterarchi- 306 cal coordinate, the plot converges to the analytical 307 solution given by [12] as also shown by [18], which 308 is found by solving the diffusion equation 309

$$\frac{\partial \phi}{\partial t} = D \frac{\partial^2 \phi}{\partial z^2}. \quad (18)$$

294 3.2 Unstructured lattice

295 After validating the heterarchical approach using 316 the idealised structured lattice, where each cell in 317

the lattice has the same volume, here we test the method on an unstructured lattice, in which the cells have varying volume.

The unstructured lattice is formed by randomly distributing points in space inside a defined boundary. The volume of these points is then obtained using the Voronoi polygon method. A number of such unstructured lattices are considered along the heterarchical coordinate, as done previously for the structured lattice. The initial and boundary conditions are the same as those used for the structured lattice. We then apply our heterarchical rules to model segregation and mixing independently for a bidisperse system. Fig. 7 shows the unstructured lattice used for testing the numerical method's capability to model bidisperse segregation and mixing. A spatiotemporal plot for the average particle size with time along the physical coordinate in the vertical direction is also shown in Fig. 8 for both the segregation and mixing mechanisms. The results replicate the

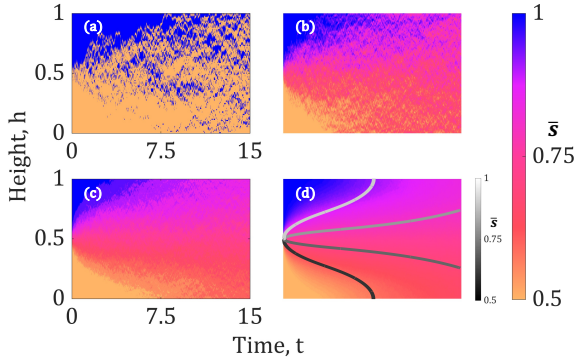


Fig. 6: Time evolution of average particle size (\bar{s}) in a structured lattice for bidisperse mixing with varying number of cells along the heterarchical coordinate (M). For all cases the diffusivity $D = 0.01 \text{ m/s}^2$ and the lattice consists of 100×100 cells along the two spatial coordinates. From (a) to (d) the number of cells along the heterarchical coordinate are varied as $M = 1, 10, 10^2$ and 10^3 . As the number of cells along the heterarchical coordinate increases the solution converges to the equivalent analytical solution of the 1D diffusion equation. *Bottom right* shows the superimposed contour lines in gray obtained from the analytical solution of the 1D diffusion equation (Eq. 18) (colour figure online).

318 corresponding results for the structured lattice
 319 and are in agreement with the analytical solution
 320 of the corresponding continuum equations for
 321 the advection and diffusion problems (Eq. 17 and
 322 Eq. 18), respectively. This validates our approach
 323 to model segregation and mixing using the heter-
 324 archical method. The next task is thus to adopt
 325 this method on the unstructured lattice used for
 326 rotary mills.

4 Rotary drums without crushing: lab-scale

327 The segregation and mixing models contain two
 328 free parameters, one controlling the rate of seg-
 329 reation (c_o) in Eq. 6 and one controlling the
 330 rate of diffusivity (l) in Eq. 9. To calibrate val-
 331 ues for these models, a qualitative comparison is
 332 made here with experimental results for mixing
 333 and segregation in the literature [25, 35].

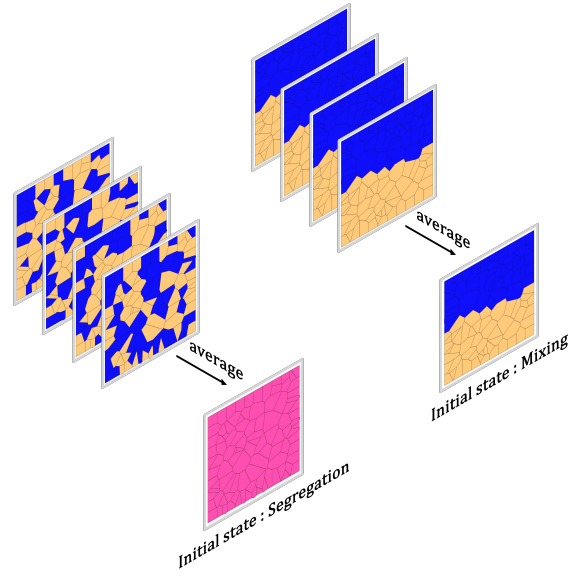


Fig. 7: Bidisperse segregation and mixing in an unstructured lattice. The cells are randomly distributed in the lattice and are filled with small (yellow) and large (blue) particles in equal proportion. A number of such lattices are considered along the heterarchical coordinate. The particle size is averaged along the heterarchical coordinate for each cell. For the segregation, we start with the initial condition of a uniform distribution of particle size in the lattice and for the mixing, we start with an initial condition of a perfectly segregated state. The rules for segregation and mixing are then applied (colour figure online).

4.1 Mixing

336 The mixing of particles in rotary drums is sim-
 337 ulated for monodispersed systems with only one
 338 particle size. For visualisation purposes, the ini-
 339 tial colour of the heterarchical cells in the system
 340 is separated into two halves of the domain, as
 341 shown in Fig. 9. Note that in the experiment [25]
 342 the particles are initially placed such that the free
 343 surface is horizontal and the drum rotates to the
 344 angle of repose (φ) of the material at the onset of
 345 avalanche, as shown in Fig. 9. The profile of the
 346 materials within the drum maintains the constant
 347 angle of repose once the avalanche is set. In the
 348 simulation, we consider this onset of avalanche as
 349 the initial state for our simulations and assume
 350 that the particles remain inclined at this slope
 351 throughout the simulation. During the simulation,

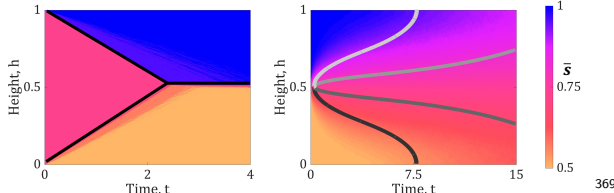


Fig. 8: Spatiotemporal plot of average particle size for bidisperse mixture in an unstructured lattice. *Left* Segregation, *Right* Mixing. For segregation, the gradient of kinetic pressure field $\nabla p_k = 1 \text{ J N/m}^3$ and for mixing, diffusivity $D = 0.01 \text{ m/s}^2$. For both cases $M = 10^3$. The superimposed lines show the corresponding analytical solution of the advection (Eq. 17) and the diffusion equation (Eq. 18) (colour figure online).

the colour of those cells is followed. Because all particles are the same size there is no segregation. Visual comparison is made with the experiments in [25] where monodispersed spherical sugar balls of two colours are mixed. The simulation parameters used to model the mixing in this rotary drum are listed in Table 1.

As detailed in Part I of this contribution, the velocity field for the granular flow in the rotary drum is derived from the analytical velocity solution given by [36]. Based on this, a set of closed streamlines were obtained, and along these, a discrete set of material points were allocated. The volumes of these material points were further discretised along the micro-structural coordinate into M cells.

To simulate the mixing mechanism, the frequency of swapping cells (here with the same particle size, though different colours) can be calculated using Eq. 15. To obtain the swapping probability, the critical time step can be calculated as done before using $\max_k (f_{i,j,s,k}^{swap}) \Delta t_c < 1/2$ for each material point, and considering the minimum value. However, in doing so, there are very few material points in the system for which the critical time step is substantially small (about $\approx 10^4$ order smaller than the rest of the points). Adopting such time step will cause the simulations to run very slowly. In order to overcome this, the critical time step for mixing (Δt_m) is taken as the volume average of the critical time steps of all the

material points in the system and is given as

$$\Delta t_m = \frac{\sum_i \sum_j \Delta t_c^{i,j} V_{i,j}}{\sum_i \sum V_{i,j}}, \quad (19)$$

where $\Delta t_c^{i,j}$ is the critical time step for the material point and $V_{i,j}$ is the volume of the material point. This choice is validated by reducing the time step further and verifying that the results do not practically vary.

Table 1: Simulation parameters for mixing [25]

Parameter	Value	Unit
Drum diameter (d)	13.8	cm
Rotational speed (ω)	4.5	rpm
Particle size (s)	1.8	mm
Density (ρ_m)	1.1	g/cm ³
Angle of repose (φ)	20.6°	degree

The diffusivity can be calculated using Eq. 9. The free parameter l in the diffusivity equation is varied here to make the model respond similar to that in the experiment. Fig. 9 shows the mixing state in the rotary drum after different drum revolutions obtained from the simulation and the experiment. Using the value of $l = 10$, which has also been adopted by [31], appears to yield a satisfactory comparison. In this comparison, we adopted $M = 1$ heterarchical cell as the experimental visuals do not show the mixing of particles along the length of the drum. To further confirm the model's continuum limit, as previously demonstrated in the previous section as well as in Part I of this study, we model mixing within the rotating drum for $M = 10^3$ heterarchical cells. The mixing state after one revolution of the drum is shown in Fig. 9i, where the particle size is averaged along the micro-structural coordinate.

4.2 Segregation

Segregation of particles by size in rotary drums has been the topic of several studies [19, 35, 37, 38]. Most studies focused on drums with binary particle sizes, from which two important observations could be made. At low rotational speeds, the drum develops transient radial streak patterns,

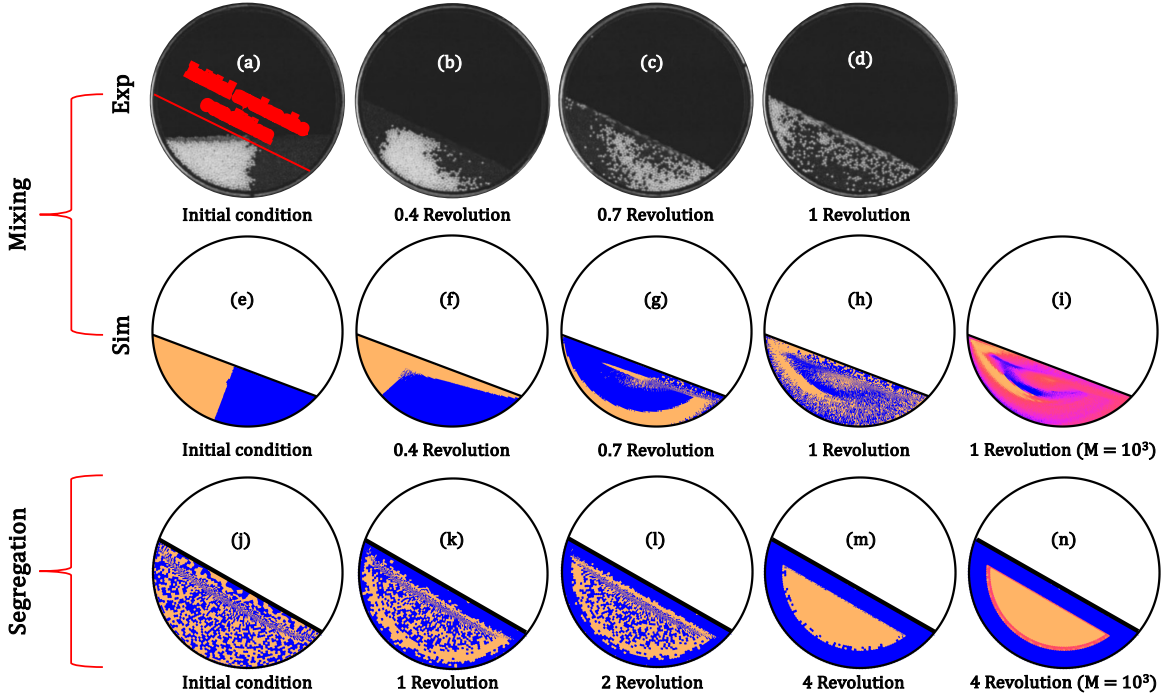


Fig. 9: Comparison of mixing and segregation for a lab scale rotating drum: (a-d) The evolution of mixing for a rotating drum in an experiment [25]. For the experimental rotating drum, the drum is initially filled in two halves using identical particle sizes coloured white and black. The particles are initially placed horizontally and as the drum rotates, the particles get inclined at the angle of repose of the material. In all simulations $M = 1$ unless specified otherwise. (e-i) Evolution of mixing in a simulated rotating drum. The drum is initially filled in two halves using identical particle sizes coloured yellow and blue. The experiment starts horizontally whereas the simulated sample begins at the initial avalanche condition. (j-n) Evolution of segregation in a simulated rotating drum. The drum is initially filled with small particles (yellow) and large particles (blue) in equal proportion and distributed uniformly in the drum. (i,n) The continuum limit of the heterarchical model is illustrated with $M = 10^3$ (colour figure online).

whose exact form depends on the degree of filling and the particle size ratio. However, at higher rotational speeds, these streaks get suppressed, while instead the system quickly develops a steady state motion with radially segregated pattern, where the smaller particles tend to occupy the inner core of the bulk. This work focuses on the high rotational speeds associated with rotary mills. Therefore, here the heterarchical approach will be adopted, to see if it can recover the radially segregated pattern in binary systems of particle sizes. In so doing, our primary objective is to calibrate the parameter (c_o), which controls the rate of segregation (see Eq. 6). The formation of radial streak formations using heterarchical approach is beyond the scope of the present study and would

Table 2: Simulation parameters for segregation [37]

Parameter	Value	Unit
Drum diameter (d)	32	cm
Rotational speed (ω)	5	rpm
Particle size (s)	1 and 2	mm
Density (ρ_m)	2.5	g/cm ³
Angle of repose (φ)	30°	degree
Degree of filling (f)	40	%

require a different approach than integration along steady state streamlines.

The work of [35] provides a particularly valuable observation for the current study. Specifically, that work illustrated the impact of the degree of

421 filling and particle size ratio on the number of
 422 revolutions required to achieve close to complete
 423 segregation of bidisperse particles in rotary drums.
 424 The simulation parameters based on [37] using
 425 glass beads for segregation in a rotating drum are
 426 listed in Table. 2. The critical simulation time
 427 step for segregation $\Delta t_s = \sum_i \sum_j \Delta t_c^{i,j} V_{i,j} / \sum V_{i,j}$
 428 is obtained by volume averaging.

429 Based on the degree of filling ($f = 40\%$) and
 430 the particle size ratio ($= 0.5$) the number of revolu-
 431 tions required for achieving complete segregation
 432 is about ≈ 4 revolutions. Fig. 9 shows the evolu-
 433 tion of the segregated state in rotary drum. The
 434 parameter controlling the rate of segregation (c_o)
 435 as defined in Eq. 6 is varied until complete segre-
 436 gation is achieved in the aforementioned number
 437 of revolutions. The calibrated value $c_0 = 0.05 \text{ s}^{-1}$
 438 is obtained from the simulations.

439 As done previously for the mixing of particles,
 440 we reaffirm the continuum limit of the heterarchi-
 441 cal model by simulating segregation in the rotat-
 442 ing drum for $M = 10^3$ number of heterarchical
 443 cells. The segregation state after four revolutions
 444 of the drum is shown in Fig. 9n, where the par-
 445 ticle size is averaged along the micro-structural
 446 coordinate.

447 With this, we now have all the model param-
 448 eters required to proceed and study how the
 449 processes of mixing and segregation may alter the
 450 extent of crushing for a polydisperse mineral flow
 451 in field-scale AG mills.

452 5 Rotary drums with 453 crushing: field-scale

454 So far we have introduced a new numerical scheme
 455 for solving the heterarchical physics that governs
 456 particle size segregation and mixing, and tested
 457 it for binary mixtures that do not involve parti-
 458 cle crushing. However, the physics that governs
 459 kinetic crushing within the heterarchical frame-
 460 work has already been defined independently in
 461 Part I. Therefore, it is now possible to study the
 462 combined effects of these three particle size mech-
 463 anisms, especially how the segregation and mixing
 464 may impact the extent of particle crushing in
 465 rotary mills. Here, we focus on the spatiotempo-
 466 ral progression of comminution within field-scale
 467 autogenous grinding (AG) mills.

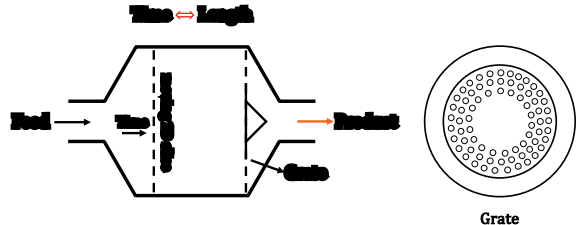


Fig. 10: Schematic of an Autogenous grinding mill and a typical grate design for the discharge of finely crushed material through the mill. Note that in the current 2-dimensional (2D) simulation for the AG mill, we use time (or mill revolution) as a proxy for the processing time of the mineral particles inside the mill.

468 To put such simulations into a practical con-
 469 text, it is important to understand the working
 470 parameters of an actual AG mill. During the AG
 471 mill operation, there is a continuous flow of mate-
 472 rial within the mill. The coarser fresh material is
 473 fed from one end of the mill and the finer crushed
 474 material gets discharged from the other end. This
 475 rate of mass flux, which in the mineral processing
 476 industry is commonly referred to as ‘throughput’,
 477 is typically maintained constant during the mill
 478 operation. The throughput of the mill is generally
 479 measured in tonnes of ore processed per hour (tph)
 480 and depends on several factors such as the ore
 481 type and hardness, mill size, as well as operating
 482 parameters [39–41]. The throughput determines
 483 the residence time of a typical mineral particle
 484 inside the mill.

485 To simulate this operation accurately, one
 486 would need to model a full 3-dimensional (3D) AG
 487 mill and follow 3D helical streamlines depicting
 488 the material’s path from the feed end to the dis-
 489 charge end. However, for simplification purposes,
 490 here we opt for a 2D representation of the flow
 491 within an AG mill, representing a moving cross-
 492 section of the mill along its length. We use the
 493 number of mill revolutions as a proxy for the pro-
 494 cessing time of the mineral inside the mill, repre-
 495 senting the flow of material along the mill length.
 496 Considering a typical throughput of 600 tph for
 497 the mill which is operating at a speed of 13.5 rpm
 498 with a total mass of 10.5 tonnes, implies that the
 499 mill is processing around 0.75 tonnes/rev of mill.
 500 Therefore, for processing a total mass of around

501 10.5 tonnes, the residence time of a typical mineral
 502 follows around 13 mill revolutions. As such,
 503 in the current study, we run the simulation for 13
 504 mill revolutions.

505 It is important to note that in this simulation,
 506 no mass flux is explicitly modelled inside the mill.
 507 The material is fed into the mill at the start of
 508 the simulation, and the crushed finer particles are
 509 removed only at the end of the simulation which
 510 in this case happens after 13 revolutions of the
 511 mill. The exit of fine material through the dis-
 512 charge end of the mill is facilitated by using a
 513 grated screen [42]. This screen consists of a series
 514 of openings distributed over its surface, and covers
 515 2–12% of the mill cross-sectional area. We consider
 516 one design of such grates from [42], which is shown
 517 in Fig. 10. The size of the grates on the screen
 518 controls the size of the fine particles filtering out
 519 of it. Once this material comes out through the
 520 grated screen, it is then passed into the discharge
 521 trunnion with the help of pulp lifters [43]. Details
 522 regarding how we measure the product particle
 523 size distribution exiting through this grated screen
 524 will be discussed later in this section.

525 The simulation parameters for the AG mill are
 526 the same as those used for the simulations in part
 527 I of this contribution, as recapped in Table. 3.
 528 The segregation velocity of the particles is still
 529 calculated using Eq. 6 where the adopted value
 530 of constant (c_o) is taken to be the same as cali-
 531 brated in Sec 4. The segregation velocity is also
 532 dependent on the gradient of the kinetic pres-
 533 sure field. The kinetic pressure field for the AG
 534 mill is obtained from the discrete element method
 535 (DEM) simulation using coarse-graining, as shown
 536 in Fig. 11a and explained in Part I of this con-
 537 tribution. The gradient of the kinetic pressure can
 538 thus be obtained. For implementing the mixing
 539 mechanism, the diffusivity field (see Fig. 11b) is
 540 calculated using Eq. 9 where the value of the
 541 constant (l) is used as calibrated in Sec 4.

542 For the case of the current simulation, the
 543 particles residing on a material point of a given
 544 streamline not only undergo crushing but also
 545 advect and diffuse in space due to segregation
 546 and mixing events. This is illustrated for the two
 547 stochastic simulations shown in Fig. 12, where the
 548 trajectory of a tracer parcel of particles is plotted
 549 over time inside the mill. As done in Part I of this
 550 contribution, when only the crushing mechanism

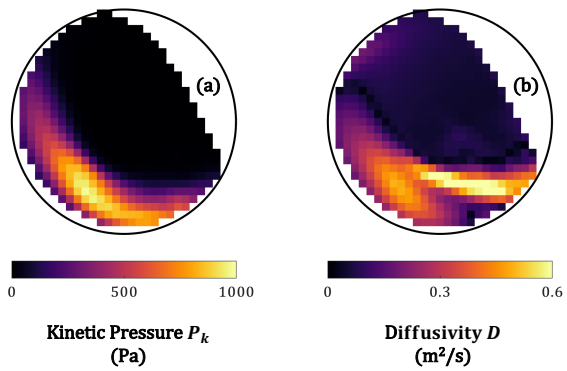


Fig. 11: Kinematics for an AG mill: (a) Coarse-grained kinetic pressure field from DEM simulation (b) Initial diffusivity field calculated using Eq. 9 (colour figure online).

551 is activated in the model, the tracer merely trav-
 552 els along its initial streamline. However, as is done
 553 here, in Part II, when the segregation and mix-
 554 ing mechanisms are activated the tracer frequently
 555 jumps between streamlines.

556 The heterarchical model allows us to track the
 557 evolution of the overall particle size distribution
 558 (PSD) inside the mill at any point in time. Fig. 13
 559 shows the evolution of PSD with different num-
 560 bers of mill revolutions. It can be seen that as
 561 the mill revolves, the minerals continually crush,
 562 producing finer and finer product. Recall that in
 563 Part I of the contribution, when only the crush-
 564 ing mechanism was activated, the PSD ceased to
 565 evolve after one revolution. In that case, the par-
 566 ticles within a material point achieved a cushioned
 567 state whereby they got protected by neighbour-
 568 ing particles, and those neighbours did not alter
 569 their size. However, in the presence of segrega-
 570 tion and mixing this cushioned state is destabilized
 571 due to the corresponding exchange of particles from
 572 fluxes between neighbouring material points.

573 The new heterarchical model also provides
 574 access to the evolution of particle size distributions
 575 in both space and time inside the AG mill. Fig. 14
 576 shows the evolution of mean particle size (d_{50}) for
 577 the whole mill domain for different revolutions of
 578 the mill (an animation showing the evolution of
 579 d_{50} can be found in SI Video 3). As shown, the
 580 simulation begins with a uniform mean particle
 581 size throughout the volume of the AG mill. How-
 582 ever, as the simulation progresses finer material

Table 3: Simulation parameters for an AG mill

	Parameters	Symbol	Value	Unit
Geometrical Parameters				
	Mill Diameter	d	6	m
	Degree of filling	f	30	%
Mechanical Parameters				
Old (taken from part I)	Rotational velocity	ω	13.5	rpm
	Material density	ρ_m	2500	kgm^{-3}
	Scaling parameter	n	0.05	
	Fragment size distribution parameters	k	4	
		λ	1	
	Crushing strength (for particle size s^m)	σ^m	50	kPa
	Weibull modulus for strength	w_s	2	
	Weibull modulus for velocity	w_v	6	
	Correlation parameters for impact velocity	a_v	1.5	ms^{-1}
		b_v	0.4	
New	Rate of segregation	c_o	0.05	s^{-1}
	Rate of diffusivity	l	10	

583 is produced all around the mill, with the coarsest 598
 584 particles concentrated in a kidney-shaped region 599
 585 within the mill. More specifically, two observations 600
 586 can be made about the comminution behaviour 601
 587 inside the AG mill. Firstly, the outer stream- 602
 588 lines predominately consist of finer particles. This 603
 589 is because the material along these streamlines 604
 590 passes through a region of high fluctuating veloc- 605
 591 ity (v') (more details on fluctuating velocity in 606
 592 the Part I paper) which leads to frequent particle 607
 593 collisions resulting in crushing. Secondly, there is 608
 594 radial segregation of particles, whereby the larger 609
 595 particles tend to migrate toward the inner region 610
 596 of the mill charge. These observations are consis- 611
 597 tent with predictions using DEM simulations and

experiments, as has been observed by [44, 45]. It is also very important to note that for the lab-scale rotary mill, which operates at a very low speed compared to the AG mill, the particle segregation behaviour is such that the smaller particles occupy the core region surrounded by larger particles on the periphery. However, for the currently studied case of the AG mill, the mean particle size plots exhibit an opposite trend where larger particles occupy the core region surrounded by smaller particles on the outside.

Specifically, in this inner region of the charge for the AG mill, the fluctuating velocities of particles are small (refer to Part I) and the collision

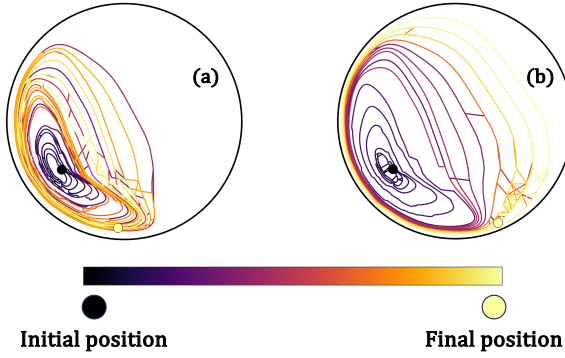


Fig. 12: Trajectory of a tracer parcel of particles for the simulation of comminution in an AG mill. The segregation and mixing events cause the tracer to move from one streamline to another. Otherwise, in the absence of segregation and mixing the tracer traverses only along its original given streamline. Panels (a) and (b) show the trajectory for the same tracer parcel of particles. The stochastic nature of the segregation and mixing mechanisms cause the tracer to follow different trajectories (colour figure online).

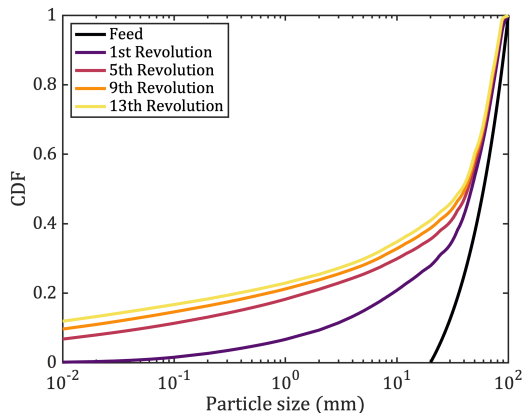


Fig. 13: Cumulative distribution function (CDF) of the product particle sizes for the whole material inside a simulated AG mill (colour figure online).

frequency is very low. Therefore, these big particles survive crushing even after the total residence time of 13 revolutions within the mill. This phenomenon has also been experimentally observed for industrial AG mills [46]. For the experimental AG mills, there is no practical way to look inside

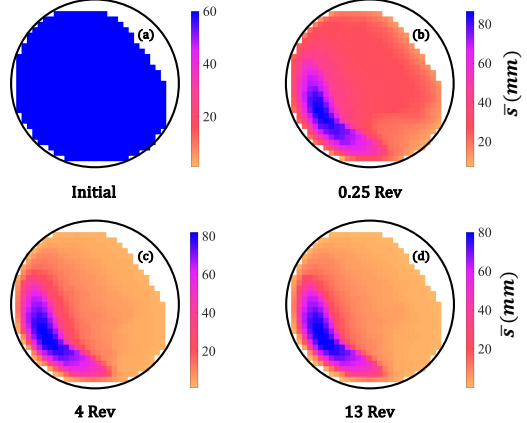


Fig. 14: Evolution of mean particle size field (d_{50}) during the simulation of comminution in an AG mill. From (a) to (d), the d_{50} at the initial state as well as after 0.25, 4, and 13 revolutions respectively (colour figure online).

the mill during its operation due to the turbulent environment. At best, researchers did actually stop the ongoing operation of the mill and emptied its content for further inspection. Powell et al. [46] crash stopped the AG mill and emptied its content to reveal the presence of bigger rocks still surviving in the mill. Our model explains why these large rocks survive crushing, even though statistically the bigger particles have lower crushing strength than the smaller particles.

Furthermore, to better understand the role of segregation and mixing in comminution, we analysed their effect on the crushing mechanism in isolation. To this end we ran simulations that implemented only one of these two open-system mechanisms, together with the crushing mechanism. Fig. 15 shows the evolution of the PSD for the simulation which activated only the crushing mechanism (from Part I), as well as crushing and mixing only, crushing and segregation only, and all three mechanisms together (the animations showing the evolution of mean particle size (d_{50}) for the case of crushing plus mixing and crushing plus segregation can be found in SI as Video 4 and Video 5). From the figure, it can be seen that when only the mixing mechanism is activated together with crushing, there is less amount of crushing as compared to the case when only the segregation mechanism is activated with crushing. Most importantly, the particle size distribution

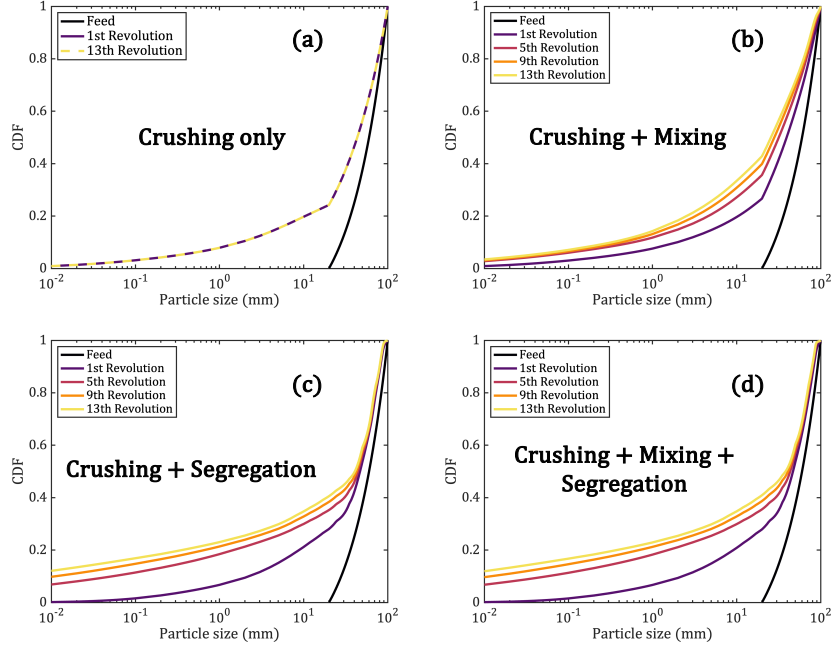


Fig. 15: Cumulative distribution function (CDF) of product particle sizes when (a) Only the crushing mechanism is activated. The system undergoes no further crushing after one revolution. (b) Only the crushing and mixing mechanism is activated. (c) Only the crushing and segregation mechanism is activated (d) Crushing, mixing, and segregation are activated together (colour figure online).

for the case of crushing plus segregation is very similar to the case whereby all three mechanisms are activated together. This implies that relative to mixing the segregation mechanism is greatly enhancing the process of comminution in rotary mills. We also note that in the case when only segregation and crushing are activated, even though the mixing mechanism is not activated directly, the system still undergoes mixing indirectly. This indirect mixing results from the different advection speeds along the different streamlines. This sort of mixing is directly related to the “Baker” mixing [47–49].

As shown in the Part I paper, the heterarchical model has a well-defined continuum limit. We saw that when the number of heterarchical cells are very large, the model predicts very smooth results. Also, we presented the numerical robustness of the method by showing that the results stabilise for simulations with anything larger than around $M = 10^2$ heterarchical cells. Although in the Part I paper, we only dealt with the crushing mechanism, and the simulation is run for only one revolution of the mill, the computational intensity

was never an issue. But in this Part II, we found that the computational cost of the model matters. In order to check the numerical robustness of the model for the current case, we ran simulations with a 10 and 100 times lower numbers of heterarchical cells and compared the results with the already obtained results. Fig. 16 shows the contour plot for the mean particle size (d_{50}) after the simulated 13 revolutions of the mill and the evolution of product size inside the mill with varying the number of heterarchical cells from a lower $M = 10^1$ to a higher $M = 10^3$. It can be seen that even with $M = 10^2$ number of heterarchical cells the model response is similar, reaffirming the robustness of the model.

Up until now, we have discussed the dynamics that is occurring inside of the AG mill. As explained earlier, the fine material is discharged from the mill using a grated screen at the end. The mechanism governing the passage of fine material through the holes in the grate screen needs to be investigated. In general, the rate of discharge of these fine particles through these holes may be a function of the size of these holes, the size of fine

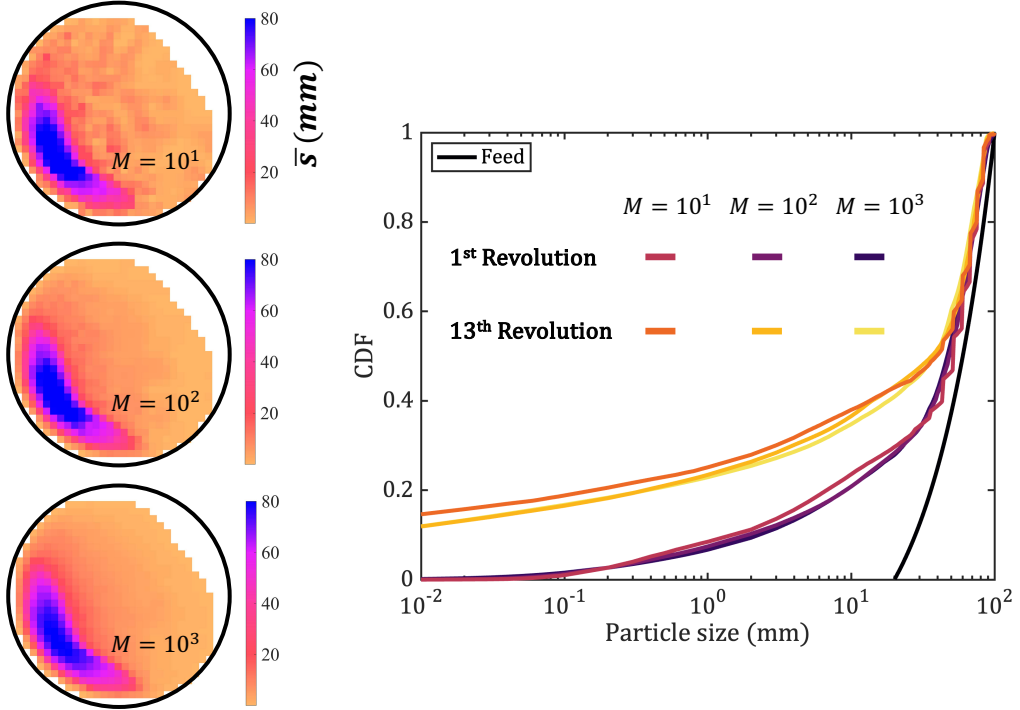


Fig. 16: Comparison of simulation result for variation in the number of heterarchical cells (M), from lowest $M = 10^1$ to highest $M = 10^3$. On the *left*, mean particle size (d_{50}) after 13 revolutions of the mill. On the *right*, the evolution of particle size distribution (colour figure online).

696 particles, the fluctuating velocity of particles, and
 697 the kinetic pressure field. At this stage, we do not
 698 delve deep into these physics and rather adopt
 699 a simple probabilistic approach that allows us to
 700 estimate the particle size distribution of the fine
 701 material that exits through the grate.

702 Specifically, we consider a grated screen that
 703 has radially distributed holes covering the region
 704 from the periphery to a certain distance from the
 705 centre, which in this case is assumed to be a dis-
 706 tance of two-thirds from the centre of the screen.
 707 These apertures are assumed to be circular and
 708 have a diameter s_g for simplicity. The effect of
 709 the shape of apertures, their distribution, and the
 710 distance from centre of the screen needs to be fur-
 711 ther investigated in the future and is beyond the
 712 present scope of this study.

Therefore, the available area (a) for a par-
 ticle of size $s \leq s_g$ to pass through this aperture is
 $a = \pi(s_g - s)^2/4$. The probability (p) of passing a
 particle of size s through the aperture of size s_g is

then,

$$p = \frac{\text{available area}}{\text{aperture area}} = \left[1 - \left\langle \frac{s}{s_g} \right\rangle \right]^2, \quad (20)$$

713 where $\langle \rangle$ is the Macaulay function. Note that
 714 the expression for probability in Eq. 20 is an
 715 approximation where we consider the probabili-
 716 ty of passing finer particles through the grate
 717 as a function of only particle size and the size
 718 of the grate. The actual physics governing this
 719 mechanism which might be additionally related
 720 to the kinetic pressure or fluctuating velocities of
 721 particles is not accounted for here.

The probability density function $P(s)$ for the
 above function can be obtained by normalising the
 function with the total area under the curve and
 can be expressed as

$$P(s) = \frac{3}{s_g} \left[1 - \left\langle \frac{s}{s_g} \right\rangle \right]^2. \quad (21)$$

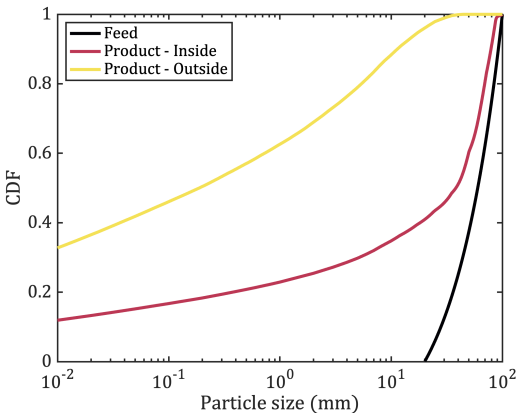


Fig. 17: Cumulative distribution function (CDF) of the product particle size inside the mill, as well as outside the mill after screening through the grates. A typical grate size of diameter $s_g = 50$ mm is considered here (colour figure online).

The mass fraction of particles with size $s \leq s_g$ is then extracted through the grated screen based on the above probability density function.

Fig. 17 shows the PSD for the product passing through the grate. In the current simulation, the discharge of the material is measured all at once after the end of the simulation. This simplified method ignores important factors that may affect the interpretation of the product PSD, such as the role of slurry pool on restricting the passage of finer material through the grate [42].

6 Conclusions

This comprehensive two-part contribution presents a novel approach for modelling comminution within rotary mills, by integrating the multiscale heterarchical stochastic physics with the streamline method. Our study tackles the inherent challenges of conventional modelling approaches applied to comminution in these mills. These challenges primarily stem from the intricate interplay of an extensive range of particles and the complex dynamics they undergo during the process.

The limitations of the existing particle-based simulations, like the discrete element method (DEM), were meticulously addressed in this contribution. Likewise, we addressed the shortcomings of simplified approaches based on population

balance models (PBM), that tend to oversimplify particle dynamics within the mills. Our approach offers a remedy by fusing heterarchy along streamlines, a novel concept that helped us make new observations regarding granular flow and comminution within rotary mills. Compared with previous models in the field, the new approach can both accommodate the massive number of particles involved in real mills, as well as facilitating a nuanced comprehension of their behaviour both temporally and locally within the mill.

The contribution of this study to the understanding of comminution is threefold. Firstly, our methodology introduces the concept of kinetic crushing, a pivotal factor in granular flow that sustain high deformations, as prevalent in rotary mills. Secondly, we proposed to integrate the heterarchical physics controlling particle sizes along streamlines, a major step elaborated in Part I of this contribution. Lastly, in this current Part II, we extended the approach to encompass particle segregation and mixing, yielding a comprehensive framework that underpins the complex progression of the comminution process.

Applying the heterarchical rules to the mechanisms of crushing, segregation, and mixing, we studied the significance of the intricate couplings between these dynamics within an autogenous grinding (AG) mill. The heterarchical streamline model provides an insightful tracking of particle size evolution across space and time within the mill's domain. One crucial finding by our study is the pronounced role of the segregation mechanism in enhancing the overall crushing within the mill. We also highlighted why larger particles tend to survive within the mill, despite their apparent statistical material vulnerability.

In addition to these significant findings, the numerical robustness of our model has been illustrated. Although the model is intrinsically stochastic, the results have been demonstrated to be deterministic, showing a well-defined continuum limit, as demonstrated by the smooth predictions it yields with increasing number of heterarchical cells. This promising approach opens the door to a more profound understanding of comminution within rotary mills, offering invaluable insights into this industrially crucial process.

Finally, one aspect in our current analysis that warrants improvement is the process by which we derived the closed streamlines for the case

of rotary mills. This step is time-consuming and relies on a manual effort. Specifically, for a given set of operating parameters for the rotary mill, we first required to obtain the coarse-grained kinematics using a DEM simulation and then manually generate a set of closed streamlines. In the future, we envisage a more generalised, automated scheme to obtain these closed streamlines by either developing an analytical velocity model for the corresponding rotary mills, or using optimisation scheme based on the coarse-grained data. Such an enhancement would make this model significantly more convenient to apply under different operating conditions of the rotary mills.

Appendix A Calibration results for rotary drums without crushing

In Section 4, we applied the heterarchical model for lab-scale rotary drums where crushing does not develop and calibrated the parameters controlling the rates of particle mixing (l) and segregation (c_o) as given by Eq. 9 and Eq. 6, respectively. The values of these parameters upon calibration were obtained to be $l = 10$ and $c_o = 0.05 \text{ s}^{-1}$ respectively. Here, we show the corresponding mixing states and segregated states for the rotary drum with variations in the values of these parameters as depicted in Fig. A1 and Fig. A2.

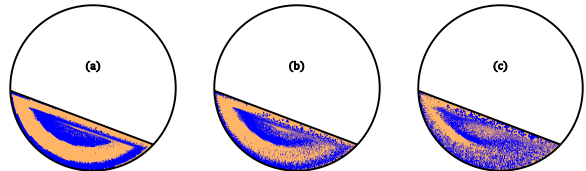


Fig. A1: Mixing states after 1 revolution for a rotating drum with variation of free parameter l , which controls the diffusivity in the system (a) $l = 0.1$ (b) $l = 1$ (C) $l = 10$ (colour figure online).

Video 1. *Caption:* An animation showing the evolution of average particle size for the case of bidisperse segregation in the structured lattice.

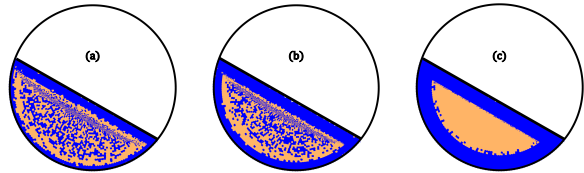


Fig. A2: Segregation state after 4 revolutions of the rotating drum for variation of the parameter c_o , which controls the rate of segregation in the system (a) $c_o = 1 \text{ s}^{-1}$ (b) $c_o = 0.1 \text{ s}^{-1}$ (c) $c_o = 0.05 \text{ s}^{-1}$ (colour figure online).

The particle size is averaged along the heterarchical coordinate for each cell in the lattice. Initially, the average particle size is uniform in each cell of the lattice. As the particles begin to segregate, we achieve a state where all the large particles move to the top and the smaller particles move to the bottom of the lattice.

Video 2. *Caption:* An animation showing the evolution of average particle size for the case of bidisperse mixing in the structured lattice. The particle size is averaged along the heterarchical coordinate coordinate for each cell in the lattice. Initially, the particles are perfectly segregated in the lattice, with bigger particles at the top and smaller particles at the bottom. As the particles begin to mix, we achieve a state of uniform average particle size in each cell of the lattice.

Video 3. *Caption:* An animation showing the evolution of mean particle size (d_{50}) in an autogenous grinding (AG) mill when all three mechanisms of crushing, mixing, and segregation mechanisms are activated.

Video 4. *Caption:* An animation showing the evolution of mean particle size (d_{50}) in an autogenous grinding (AG) mill when only crushing and mixing mechanisms are activated.

Video 5. *Caption:* An animation showing the evolution of mean particle size (d_{50}) in an autogenous grinding (AG) mill when only crushing and segregation mechanisms are activated.

Supplementary information. The online version of this article contains supplementary material, which is available to authorised users.

Acknowledgements. The authors would like to thank Molycop and The University of Sydney for financially supporting this project.

870 References

- 871 [1] A. Billi, On the extent of size range and power
872 law scaling for particles of natural carbon-
873 ate fault cores. *Journal of Structural Geology*
874 **29**(9), 1512–1521 (2007)
- 875 [2] A. Billi, Grain size distribution and thickness
876 of breccia and gouge zones from thin (< 1 m)
877 strike-slip fault cores in limestone. *Journal of*
878 *Structural Geology* **27**(10), 1823–1837 (2005)
- 879 [3] P. Bartelt, B.W. Mcardell, Granulometric
880 investigations of snow avalanches. *Journal of*
881 *Glaciology* **55**(193), 829–833 (2009)
- 882 [4] C.J. Phillips, T.R. Davies, Determining rhe-
883 ological parameters of debris flow material.
884 *Geomorphology* **4**(2), 101–110 (1991)
- 885 [5] H.U. Schmincke, Graded lahars in the type
886 sections of the ellensburg formation, south-
887 central washington. *Journal of Sedimentary*
888 *Research* **37**(2), 438–448 (1967)
- 889 [6] S. Dunning, The grain size distribution of
890 rock-avalanche deposits in valley-confined
891 settings. *Italian Journal of Engineering Geol-*
892 *ogy and Environment* **1**, 117–121 (2006)
- 893 [7] N. Pollet, J.L. Schneider, Dynamic disinte-
894 gration processes accompanying transport of
895 the holocene flims sturzstrom (swiss alps).
896 *Earth and Planetary Science Letters* **221**(1-
897 4), 433–448 (2004)
- 898 [8] H.A. Makse, P. Cizeau, H.E. Stanley, Possi-
899 ble stratification mechanism in granular mix-
900 tures. *Physical review letters* **78**(17), 3298
901 (1997)
- 902 [9] S. Savage, C. Lun, Particle size segregation in
903 inclined chute flow of dry cohesionless gran-
904 ular solids. *Journal of fluid mechanics* **189**,
905 311–335 (1988)
- 906 [10] V. Dolgunin, A. Kudy, A. Ukolov, Develop-
907 ment of the model of segregation of particles
908 undergoing granular flow down an inclined
909 chute. *Powder technology* **96**(3), 211–218
910 (1998)
- 911 [11] J. Gray, A. Thornton, A theory for parti-
912 cle size segregation in shallow granular free-
913 surface flows. *Proceedings of the Royal Soci-
914 ety A: Mathematical, Physical and Engineer-
915 ing Sciences* **461**(2057), 1447–1473 (2005)
- 916 [12] J. Gray, V. Chugunov, Particle-size segrega-
917 tion and diffusive remixing in shallow granu-
918 lar avalanches. *Journal of Fluid Mechanics*
919 **569**, 365–398 (2006)
- 920 [13] J. Gray, C. Ancey, Multi-component
921 particle-size segregation in shallow granular
922 avalanches. *Journal of Fluid Mechanics* **678**,
923 535–588 (2011)
- 924 [14] Z. Deng, P.B. Umbanhowar, J.M. Ottino,
925 R.M. Lueptow, Continuum modelling of seg-
926 regating tridisperse granular chute flow.
927 *Proceedings of the Royal Society A: Mathe-
928 matical, Physical and Engineering Sciences*
929 **474**(2211), 20170384 (2018)
- 930 [15] B. Marks, P. Rognon, I. Einav, Grainsize
931 dynamics of polydisperse granular segregations
932 down inclined planes. *Journal of Fluid*
933 *Mechanics* **690**, 499–511 (2012)
- 934 [16] B. Marks, I. Einav, A mixture of crushing and
935 segregation: the complexity of grainsize in
936 natural granular flows. *Geophysical Research*
937 *Lettters* **42**(2), 274–281 (2015)
- 938 [17] C.P. Schlück, A.B. Isner, B.J. Freireich,
939 Y. Fan, P.B. Umbanhowar, J.M. Ottino, R.M.
940 Lueptow, A continuum approach for predict-
941 ing segregation in flowing polydisperse granu-
942 lar materials. *Journal of Fluid Mechanics*
943 **797**, 95–109 (2016)
- 944 [18] B. Marks, I. Einav, A heterarchical multi-
945 scale model for granular materials with evolv-
946 ing grainsize distribution. *Granular Matter*
947 **19**(3), 61 (2017)
- 948 [19] Z. Deng, P.B. Umbanhowar, J.M. Ottino,
949 R.M. Lueptow, Modeling segregation of poly-
950 disperse granular materials in developing and
951 transient free-surface flows. *AIChE Journal*
952 **65**(3), 882–893 (2019)

- 953 [20] Z. Deng, Y. Fan, J. Theuerkauf, K.V. Jacob, P.B. Umbanhowar, R.M. Lueptow, Modeling segregation of polydisperse granular materials in hopper discharge. *Powder Technology* **374**, 389–398 (2020)
- 954 [21] J.M.N.T. Gray, Particle segregation in dense granular flows. *Annual review of fluid mechanics* **50**, 407–433 (2018)
- 955 [22] B. Zanuttigh, A. Di Paolo, Experimental analysis of the segregation of dry avalanches and implications for debris flows. *Journal of Hydraulic Research* **44**(6), 796–806 (2006)
- 956 [23] B. Chopard, M. Droz, Cellular automata model for the diffusion equation. *Journal of statistical physics* **64**, 859–892 (1991)
- 957 [24] B. Utter, R.P. Behringer, Self-diffusion in dense granular shear flows. *Physical Review E* **69**(3), 031308 (2004)
- 958 [25] D. Khakhar, J. McCarthy, T. Shinbrot, J. Ottino, Transverse flow and mixing of granular materials in a rotating cylinder. *Physics of Fluids* **9**(1), 31–43 (1997)
- 959 [26] D. Khakhar, Rheology and mixing of granular materials. *Macromolecular Materials and Engineering* **296**(3-4), 278–289 (2011)
- 960 [27] V. Dolgunin, A. Ukolov, Segregation modeling of particle rapid gravity flow. *Powder technology* **83**(2), 95–103 (1995)
- 961 [28] K.M. Hill, Y. Fan, Granular temperature and segregation in dense sheared particulate mixtures. *KONA Powder and Particle Journal* **33**, 150–168 (2016)
- 962 [29] B. Marks, J.A. Eriksen, G. Dumazer, B. Sandnes, K.J. Måløy, Size segregation of intruders in perpetual granular avalanches. *Journal of Fluid Mechanics* **825**, 502–514 (2017). <https://doi.org/10.1017/jfm.2017.419>
- 963 [30] P. Kharel, P. Rognon, Vortices enhance diffusion in dense granular flows. *Physical review letters* **119**(17), 178001 (2017)
- 964 [31] P. Kharel, P. Rognon, Shear-induced diffusion in non-local granular flows. *Europhysics Letters* **124**(2), 24002 (2018)
- 965 [32] F. Da Cruz, S. Emam, M. Prochnow, J.N. Roux, F. Chevoir, Rheophysics of dense granular materials: Discrete simulation of plane shear flows. *Physical Review E* **72**(2), 021309 (2005)
- 966 [33] N. Ahuja, Dot pattern processing using voronoi neighborhoods. *IEEE Transactions on Pattern Analysis and Machine Intelligence* **3**(3), 336–343 (1982)
- 967 [34] B. Marks, I. Einav, A cellular automaton for segregation during granular avalanches. *Granular Matter* **13**, 211–214 (2011)
- 968 [35] D. Eskin, H. Kalman, A numerical parametric study of size segregation in a rotating drum. *Chemical Engineering and Processing: Process Intensification* **39**(6), 539–545 (2000)
- 969 [36] Y. Ding, R. Forster, J. Seville, D. Parker, Segregation of granular flow in the transverse plane of a rolling mode rotating drum. *International Journal of Multiphase Flow* **28**(4), 635–663 (2002)
- 970 [37] D. Khakhar, A.V. Orpe, J. Ottino, Continuum model of mixing and size segregation in a rotating cylinder: concentration-flow coupling and streak formation. *Powder technology* **116**(2-3), 232–245 (2001)
- 971 [38] I. Zuriguel, J. Gray, J. Peixinho, T. Mullin, Pattern selection by a granular wave in a rotating drum. *Physical Review E* **73**(6), 061302 (2006)
- 972 [39] A.P. van der Westhuizen, M.S. Powell, in *Proceedings of SAG* (2006), pp. 217–232
- 973 [40] M. Powell, A. Van der Westhuizen, A. Mainza, Applying grindcurves to mill operation and optimisation. *Minerals Engineering* **22**(7-8), 625–632 (2009)
- 974 [41] M. Bueno, T. Kojovic, M. Powell, F. Shi, Multi-component ag/sag mill model. *Minerals Engineering* **43**, 12–21 (2013)

- 1036 [42] S. Latchireddi, S. Morrell, Slurry flow in
1037 mills: grate-only discharge mechanism (part-
1038 1). Minerals Engineering **16**(7), 625–633
1039 (2003)
- 1040 [43] S. Latchireddi, S. Morrell, Slurry flow in
1041 mills: grate-pulp lifter discharge systems
1042 (part 2). Minerals engineering **16**(7), 635–642
1043 (2003)
- 1044 [44] P.W. Cleary, R. Morrisson, S. Morrell, Com-
1045 parison of dem and experiment for a scale
1046 model sag mill. International Journal of
1047 Mineral Processing **68**(1-4), 129–165 (2003)
- 1048 [45] Z. Rogovin, J. Herbst, Charge motion in
1049 a semi-autogenous grinding mill. Mining,
1050 Metallurgy & Exploration **6**, 18–23 (1989)
- 1051 [46] M. Powell, I. Govender, A. Mainza,
1052 D. Weatherley, M. Tavares, Developing a
1053 mill transport model
- 1054 [47] J.M. Ottino, Mixing, chaotic advection, and
1055 turbulence. Annual Review of Fluid Mechan-
1056 ics **22**(1), 207–254 (1990)
- 1057 [48] S. Wiggins, J.M. Ottino, Foundations of
1058 chaotic mixing. Philosophical Transactions of
1059 the Royal Society of London. Series A: Math-
1060 ematical, Physical and Engineering Sciences
1061 **362**(1818), 937–970 (2004)
- 1062 [49] I.C. Christov, R.M. Lueptow, J.M. Ottino,
1063 Stretching and folding versus cutting and
1064 shuffling: An illustrated perspective on mix-
1065 ing and deformations of continua. American
1066 Journal of Physics **79**(4), 359–367 (2011)